

# Structure of the mechanically activated ion channel Piezo1

Kei Saotome<sup>1,2</sup>, Swetha E. Murthy<sup>1</sup>, Jennifer M. Kefauver<sup>1,2</sup>, Tess Whitwam<sup>1</sup>, Ardem Patapoutian<sup>1,2</sup> & Andrew B. Ward<sup>2</sup>

**Piezo1 and Piezo2 are mechanically activated ion channels that mediate touch perception, proprioception and vascular development. Piezo proteins are distinct from other ion channels and their structure remains poorly defined, which impedes detailed study of their gating and ion permeation properties. Here we report a high-resolution cryo-electron microscopy structure of the mouse Piezo1 trimer. The detergent-solubilized complex adopts a three-bladed propeller shape with a curved transmembrane region containing at least 26 transmembrane helices per protomer. The flexible propeller blades can adopt distinct conformations, and consist of a series of four-transmembrane helical bundles that we term Piezo repeats. Carboxy-terminal domains line the central ion pore, and the channel is closed by constrictions in the cytosol. A kinked helical beam and anchor domain link the Piezo repeats to the pore, and are poised to control gating allosterically. The structure provides a foundation to dissect further how Piezo channels are regulated by mechanical force.**

The conversion of mechanical force into cellular signals, or mechanotransduction, is an essential biological function that is conserved throughout evolution. Mechanically activated channels confer force sensitivity to cells and organisms by allowing the passage of ions across the membrane in response to a mechanical stimulus<sup>1</sup>. Piezo1 and Piezo2 were identified in 2010 as a conserved class of eukaryotic mechanically activated ion channels<sup>2,3</sup> that are involved in various mechanotransduction pathways, including touch sensation<sup>4</sup>, proprioception<sup>5</sup>, nociception<sup>6</sup>, vascular development<sup>7</sup> and breathing<sup>8</sup>. In humans, gain-of-function (GOF) mutations in Piezo1 are linked to dehydrated hereditary stomatocytosis<sup>9–12</sup>, a disease in which red blood cells are dehydrated and have increased permeability to cations, and GOF mutations in Piezo2 are associated with distal arthrogyrosis<sup>13</sup>. Loss-of-function mutations in Piezo1 and Piezo2 are linked to congenital lymphatic dysplasia<sup>14</sup> and defective touch perception and proprioception<sup>15–17</sup>, respectively. Piezo proteins are structurally unrelated to other proteins, and are uniquely large compared to other ion channels (more than 2,000 amino acids). Electrophysiological studies have demonstrated that Piezo1 ion channels are gated directly by changes in membrane tension<sup>18–20</sup>, but the structural bases of mechanosensitivity and ion conduction in Piezo channels remain unknown. Previous crystallographic<sup>21,22</sup> and medium-resolution cryo-electron microscopy (cryo-EM)<sup>22</sup> studies have suggested the overall architecture of Piezo proteins. However, a mechanistic understanding of Piezo function requires high-resolution structural information of the channel.

## Cryo-EM sample and structure determination

A previous cryo-EM reconstruction of mouse Piezo1<sup>22</sup> lacked amino acid side-chain definitions and connectivity of resolved regions, precluding building of an accurate structural model. Here, we optimized Piezo1 sample preparation parameters to make Piezo1 amenable to high-resolution single particle cryo-EM structure determination (Extended Data Fig. 1). After computationally sorting particle heterogeneity (Extended Data Fig. 2a), we identified a subset of particles that were refined into both asymmetric and C3-symmetry-imposed maps of the mouse Piezo1 trimer, with overall resolutions of 4.5 and 3.9 Å, respectively. We conducted masked refinement of the central ‘core’

(Extended Data Fig. 2b–d) and C3-symmetry expansion followed by masked classification and refinement (Extended Data Fig. 3) to improve densities proximal to the central three-fold axis and the protein periphery, respectively. Both the 3.8 Å resolution core-masked map and a 4.1 Å resolution symmetry-expanded map (blade class 1) were used to build and refine a molecular model of mouse Piezo1 that spans structured regions of residues 1134–2544, including 14 transmembrane (TM) helices per protomer and other conserved C-terminal domains (Extended Data Fig. 4, Extended Data Table 1, Supplementary Data 1).

## Piezo1 core architecture

The homotrimeric Piezo1 complex exhibits a three-blade propeller shape with an extracellular ‘cap’ domain at the top of the central axis (Fig. 1), consistent with the previous medium-resolution cryo-EM reconstruction<sup>22</sup> (Extended Data Fig. 5a–c). The transmembrane region can be approximated by the weak density corresponding to the detergent micelle (Fig. 1a, b), in agreement with the hydrophobicity of the membrane-exposed amino acids in our model (Fig. 1c). Interestingly, the transmembrane region has a pronounced bend, suggesting Piezo1-induced local distortion of the membrane. Although we cannot rule out the possibility that the bending is a product of detergent solubilization, protein-induced membrane curvature has also been proposed for mechanosensitive channels of the two-pore potassium<sup>23</sup> and bacterial MscS<sup>24,25</sup> families.

The Piezo1 core (Fig. 1d–f) defines an architecture that is unique from other membrane proteins of known structure. The inner and outer transmembrane helices lie closest to the central axis, and are intervened by the extracellular cap, the structure of which was determined previously by X-ray crystallography<sup>21,22</sup>. In isolation, the trimeric arrangement of inner and outer helices and cap domains bear structural resemblance to acid-sensing ion channels<sup>26</sup> and P2X receptors<sup>27</sup>, as noted previously<sup>28</sup>. The 12 transmembrane helices peripheral to the inner and outer transmembrane helices can be grouped into three four-transmembrane-helix-containing bundles, each with the same topology, that we term Piezo repeats A, B and C, according to proximity to the central axis. Piezo repeat A of one protomer is adjacent to the outer helix of a different protomer, producing a ‘domain-swapped’ arrangement analogous to some tetrameric

<sup>1</sup>Howard Hughes Medical Institute, Department of Neuroscience, The Scripps Research Institute, La Jolla, California 92037, USA. <sup>2</sup>Department of Integrative Structural and Computational Biology, The Scripps Research Institute, La Jolla, California 92037, USA.

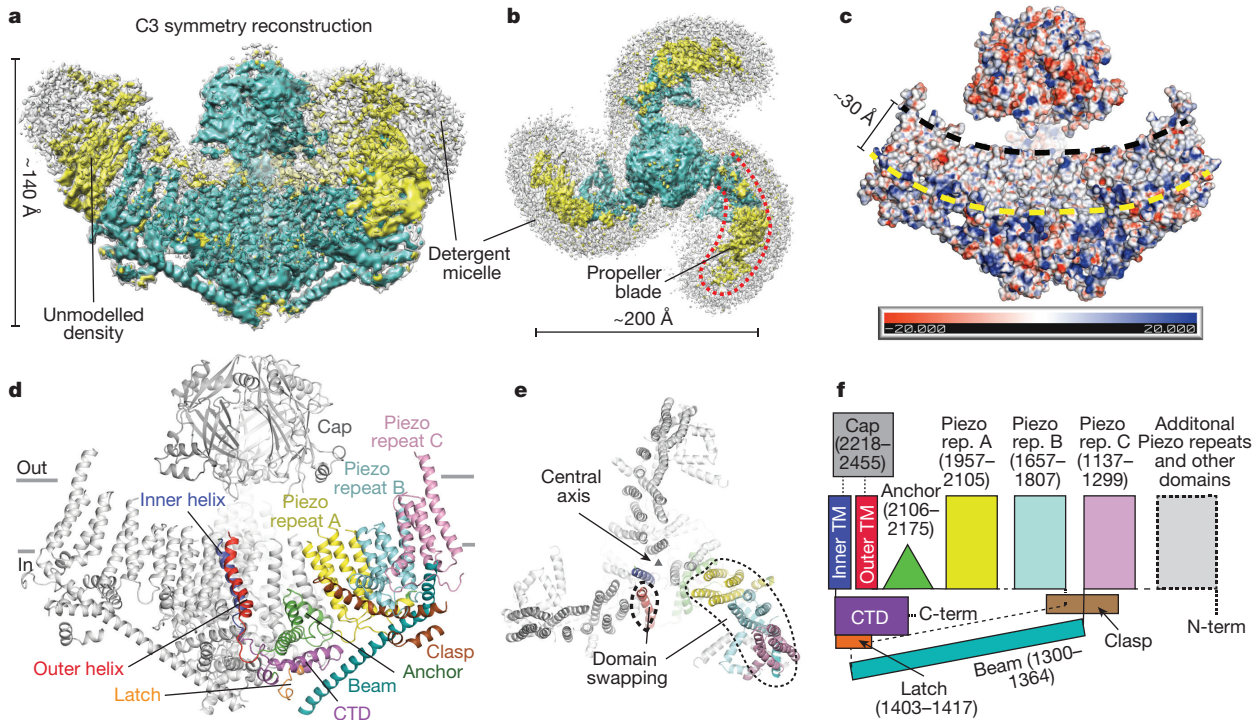


**Figure 1 | Architecture and domain arrangement of the Piezo1 core.** **a, b**, Side (**a**) and top (**b**) views of the Piezo1 cryo-EM map refined with C3 symmetry imposed. Density corresponding to modelled regions is coloured green. Less resolved density that was not modelled is coloured yellow. At lower thresholds (transparent grey map), scattered density probably originating from a detergent micelle can be observed. **c**, Surface electrostatics of the Piezo1 core model. Note the bent hydrophobic stripe representing the transmembrane region. Dotted lines approximate

ion channels<sup>29,30</sup> (Fig. 1e). The ‘anchor’ domain forms a triangular three-helix wedge between the inner and outer transmembrane helices and Piezo repeat A. The C-terminal domain (CTD) connects to the intracellular end of the inner helices, collaring the central axis. The intracellular ‘beam’, is an approximately 64-residue (~95 Å) kinked helix that runs nearly parallel to the membrane, directly underneath Piezo repeats A to C. Although the N terminus of each beam is tethered directly to Piezo repeat C, its C terminus projects towards the central axis and is connected via a roughly 37-residue disordered linker to a short, coiled peptide that we term the ‘latch’, which contacts the intracellular face of the CTDs. The latch then connects back to Piezo repeat B via a relatively non-conserved 240-residue stretch of peptide (Supplementary Data 1) that is not resolved in our maps. The beam and latch are positioned to transmit conformational changes from the propeller blade periphery to the central ion channel. The beam may also be influenced by a nearby domain that we term the ‘clasp’ (Fig. 1d, f), which was modelled without amino acid assignment owing to lower resolution and discontinuity with other domains.

### Flexible blades consist of at least six Piezo repeats

Blade-focused classification and refinement of symmetry-expanded particles yielded two classes (blade class 1 and 2) with improved density at the periphery (Extended Data Fig. 3). Remarkably, in each of these maps, clear density for an additional three Piezo repeats is resolved (Fig. 2a, b). Thus, a total of six Piezo repeats (which we have named A–F ordered by proximity to the central axis), or 26 transmembrane helices per protomer (including the inner and outer helices) are apparent, in disagreement with a previous cryo-EM study<sup>22</sup>, which proposed 14 transmembrane helices. We note the possibility of additional transmembrane helices, and potentially Piezo repeats, in the Piezo1 protein

the extracellular (black) and cytosolic (yellow) membrane boundaries. **d, e**, Side (**d**) and top (**e**) views of the Piezo1 core in cartoon representation, with each domain coloured differently. In **e**, the cap domain is removed to highlight domain swapping between Piezo repeat A and the outer helix. **f**, Schematic of the Piezo1 core domain arrangement. Dotted lines represent flexible regions that were not clearly resolved in the density maps. TM, transmembrane domain; rep., repeat; C-term, C terminus.

that were not resolved in our maps, but have been predicted bioinformatically<sup>31</sup>.

Although we were only able to place amino acids confidently for Piezo repeats A–C, the topology of the peripheral three repeats is resolved and indicates that all six have the same overall structure and arrangement of transmembrane helices (Fig. 2c, d). The termini of each repeat are cytoplasmic, with a pair of short linkers connecting the N-terminal transmembrane helices, and an extended extracellular linker connecting the third and fourth transmembrane helices. A notable feature of the Piezo repeats is the presence of cytoplasmic membrane-parallel helices tethered to their N termini. In addition to the Piezo repeats, the clasp domain also contributes a membrane-parallel helix, adjacent to that of Piezo repeat B (Fig. 2b). Amino acid assignment for the helices in Piezo repeats A, B and C demonstrates their amphipathic nature (Extended Data Fig. 6a–d). Interestingly, amphipathic helices are thought to sense or induce membrane curvature in various proteins<sup>32</sup>, and have been proposed to be crucial for membrane tension-induced gating in various classes of mechanically activated channels<sup>33</sup>. That the amphipathic helices dictate local membrane deformation, and perhaps mechanosensitivity of Piezo1 is an intriguing possibility. We speculate the array of amphipathic helices in each blade may work together to invoke a local membrane environment with continued curvature, thereby contributing to the puckered architecture.

Our blade-focused classification of the symmetry-expanded particles yielded two classes with distinct conformations demonstrating conformational flexibility of the blade. While the central regions are relatively static, the peripheral regions undergo horizontal movement in the plane of the membrane, not vertically in and out of the membrane (Fig. 2e, Extended Data Fig. 5f, g). Interestingly, associated with this lateral flexibility is an approximately 5° pivoting of the beam at a kink

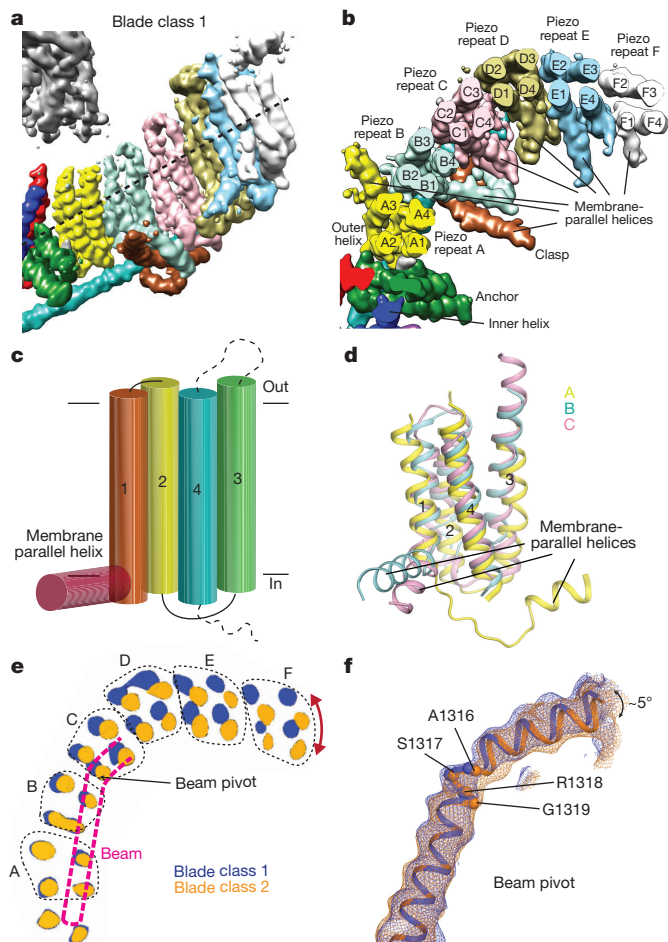


**Figure 2 | Propeller blade composition and conformational heterogeneity.** **a, b,** Side (**a**) and top (**b**) views of blade class 1 cryo-EM map, with individual domains segmented and coloured uniquely. In **b**, the map is sliced along the dotted line in **a** to highlight the positions of the transmembrane helices. **c,** Schematic of the Piezo repeat topology, which includes a cytosolic membrane parallel helix and four transmembrane helices. **d,** Aligned models for Piezo repeats A (yellow), B (cyan) and C (pink). **e,** Sagittal slice of electron density corresponding to the transmembrane region of blade class 1 (blue) and blade class 2 (orange). Approximate trajectory of the beam is shown as pink dotted line. Individual Piezo repeats are circled by black dotted lines and labelled A–F. Red double arrow depicts direction of conformational change between the two classes. **f,** Superposed cryo-EM maps and cartoon models corresponding to beam domains of blade class 1 (blue) and blade class 2 (orange). C<sub>α</sub> positions of the conserved Ala-Ser-Arg-Gly motif at the beam pivot are shown as spheres.

centred on a highly conserved Ala-Ser-Arg-Gly motif (A1316–G1319) (Fig. 2f, Supplementary Data 1). This pivot may be an important structural feature that regulates how membrane-tension-induced conformational changes at the periphery are transmitted through the beam to the central gating machinery.

### Ion-conducting pore

The extracellular cap domain, inner helix and cytosolic CTD line the central pore axis of Piezo1. Extracellular cations could approach the pore entryway vertically through the internal cavity along the three-fold axis of the cap domain, or laterally through gaps between flexible linkers connecting the cap and inner and outer helices (Fig. 3a). The cap domain, which is flexibly linked to the transmembrane domain, might have a role in mediating ion accessibility to the pore, as suggested previously<sup>28</sup>. Indeed, a comparison of our current structure to the

previous Piezo1 structure indicates distinct orientations of the cap domain and inner and outer helices (Extended Data Fig. 5d, e), illustrating the flexibility of the cap and the associated transmembrane helices.

Below the cap, the ion conduction pathway is lined by the three inner transmembrane helices. Notably, we find two lateral openings between the inner helices separated by a ‘seal’ formed by K2479 and F2480 (Fig. 3b). We term these openings the upper crevice (approximately 11 Å wide and 16 Å tall) and lower fenestration (10 Å wide and 12 Å tall), which may provide pore access for lipids or other hydrophobic molecules as a means to regulate ion conduction, reminiscent of the proposed force-gating mechanism of mechanically activated two-pore potassium channels<sup>23</sup>. Molecular dynamics simulations of the homotrimeric ATP-gated P2X3 receptor<sup>34</sup> revealed that a lower fenestration provides a passageway for ion flow into the cytoplasm. Although the possibility that the Piezo1 lower fenestration represents an ion permeation pathway warrants further study, we assume that, like most other ion channels, the pore is coincident with the central vertical axis. The pore-facing residues of the inner helices are mainly hydrophobic (Fig. 3d). The 35 Å-long membrane-spanning segment of the pore is relatively wide (more than 2 Å van der Waals radius) and does not house the narrowest constrictions of the conduction pathway (Fig. 3c, d). Instead, the ion conduction pathway narrows directly below the lower membrane boundary into a cytosolic ~11 Å long ‘neck’ (with a minimum van der Waals radius less than 1 Å) that defines the closed state of the pore in the current structure.

At the top of the cytosolic neck, the side chains of M2493 and F2494, which are conserved across Piezo orthologues (Supplementary Data 1), form a hydrophobic barrier (Fig. 3e). To examine the functional role of the apparent hydrophobic barrier, we recorded mechanically activated currents (Fig. 3g, h) from Piezo1-knockout HEK293T cells<sup>14</sup> expressing the alanine substitution mutants M2493A, F2494A and M2493A/F2494A. The double mutant M2493A/F2494A resulted in a non-functional channel despite proper trimeric assembly and surface expression (Extended Data Fig. 7a–c), demonstrating the importance of these residues. Both of the single mutants expressed as functional channels, with F2494A having significantly slower inactivation kinetics than wild-type Piezo for mechanically activated macroscopic currents in cell-attached and whole-cell configurations (Fig. 3g, h). Furthermore, stretch-activated currents from F2494A had greater steady state currents relative to wild type (Fig. 3i, Extended Data Table 2). The increased channel activity of F2494A in these recordings is consistent with this residue having a role in gating, possibly by stabilizing a non-conducting state of the channel. The M2493A mutant did not show altered permeation properties, whereas the F2494A mutant only exhibited modestly increased single channel conductance (Extended Data Fig. 7d, e) and slightly altered ion selectivity (Extended Data Fig. 7f, g, Extended Data Table 2). Our results implicate the hydrophobic barrier as an important contributor to the gating properties of Piezo1, with a minor role in determining ion conduction and selectivity. In previous studies, mutation of acidic residues (E2495 and E2496) adjacent to M2493/F2494 (Fig. 3e) affected pore properties<sup>28</sup>, suggesting that they might coordinate permeating cations. In the current structure, these residues do not project into the pore (Fig. 3e), although structural changes associated with gating could result in this region adopting conformation(s) in which the side chains of E2495 and/or E2496 face the pore to form cation-binding site(s).

Directly below the hydrophobic barrier formed by M2493 and F2494, the pore pathway narrows into a second constriction delineated by P2536 and E2537 (Fig. 3f), which are located at the turn of a helix–turn–helix motif in the distal CTD. The side chain of E2537 forms a possible hydrogen bond with Y1412 of the latch domain (Fig. 3f), which may allosterically couple movement of the latch to pore structure in this region. Approximately 4 Å below E2537 a robust density that cannot be reliably modelled but probably originates from the Piezo peptide is present (Fig. 3d). This density, which forms a cytosolic ‘plug’ to the ion channel pore, could also have a role in the permeation pathway.

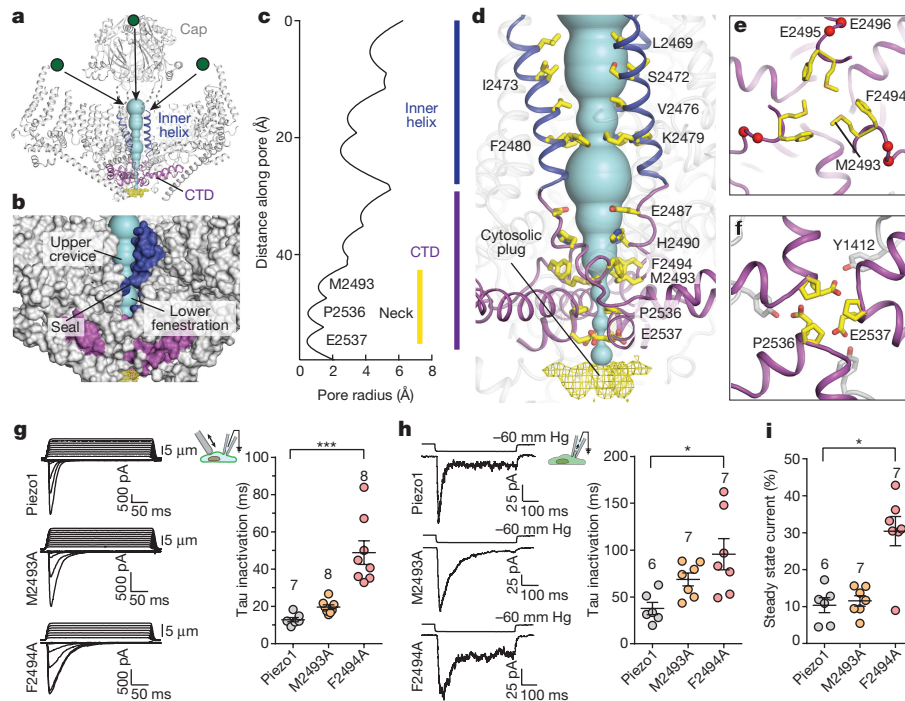


**Figure 3 | Ion pore structure and electrophysiological characterization of M2493A and F2494A.** **a**, Cartoon model of Piezo1, with the inner helix and CTD coloured blue and purple, respectively. Flexible linkers between the cap domain and the transmembrane region are depicted as dotted lines. Green spheres represent ions, with possible entryways into the pore shown as black arrows. **b**, Surface representation of the transmembrane region of Piezo1 surrounding the central axis, highlighting lateral membrane openings to the pore pathway. **c**, van der Waals radii of the pore, plotted against distance along the pore axis. The radial distance between the pore axis and the protein surface is shown as a cyan surface in **a**, **b** and **d**. **d**, Expanded view of the Piezo1 pore, with residues lining the pore pathway shown in yellow and labelled. Electron density corresponding to a ‘cytosolic plug’ is shown as a yellow mesh. **e**, **f**, Expanded top-down views of constrictions formed by M2493 and F2494 (**e**) and P2536 and E2537 (**f**). Residues mentioned in the text are also labelled. **g**, Left, representative traces of probe displacement

and mechanically activated whole-cell currents recorded ( $-80$  mV) from one cell expressing wild-type, M2493A or F2494A mouse Piezo1 channels. Right, inactivation time constant for individual cells across different conditions (Piezo1  $n = 7$  cells, M2493A  $n = 8$  cells and F2494A  $n = 8$  cells).  $***P = 0.0001$ , one-way analysis of variance (ANOVA) with Dunn’s multiple comparison test. **h**, Left, representative traces of stretch-activated macroscopic currents recorded ( $-80$  mV) in response to  $-60$  mm Hg pressure from one cell expressing wild-type, M2493A or F2494A Piezo1 channels. Right, inactivation time constant (at  $-60$  mm Hg) for individual cells across different conditions.  $*P = 0.008$ , one-way ANOVA with Dunn’s multiple comparison test. **i**, Percentage steady state current (at  $-60$  mm Hg) for individual cells across different conditions.  $*P = 0.012$ , one-way ANOVA with Dunn’s multiple comparison test. In **h** and **i**, Piezo1  $n = 7$  cells, M2493A  $n = 8$  cells and F2494A  $n = 8$  cells. Data in **g–i** denote mean  $\pm$  s.e.m.

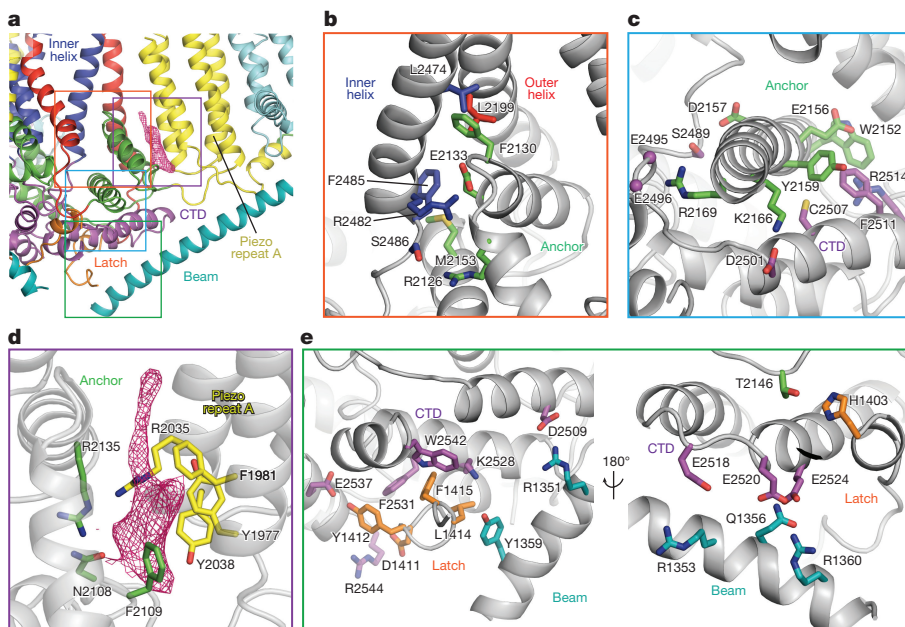


**Figure 4 | Interdomain interactions and lipid pocket.** **a**, Cartoon model of Piezo1, with colour-coded boxes around regions expanded in **b–e**. In **a** and **d**, the red mesh shows electron density corresponding to putative

lipid. In **a–e**, residues that contribute to interdomain contacts (**b**, **c** and **e**) or putative lipid binding (**d**) are shown as sticks and coloured according to domain.

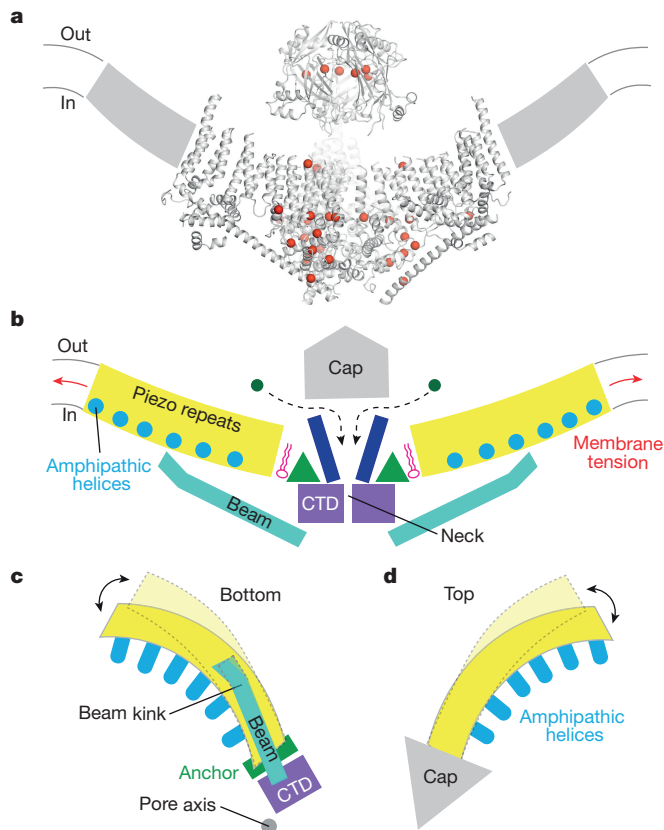


**Figure 5 | Mapping of disease mutants and schematic diagram of Piezo1 structure and conformational flexibility.** **a**, Model of the Piezo1 core, with C $\alpha$  positions of Piezo1 and Piezo2 human GOF disease mutants shown as red spheres. **b–d**, Schematic diagrams of the various Piezo1 structural elements that contribute to its function as a membrane-tension-gated channel. In **c** and **d**, bottom-up (**c**) and top-down (**d**) views of a single Piezo1 propeller blade are shown, with dotted lines and arrows depicting lateral conformational flexibility, which may be involved in gating.

### Gating machinery and lipid pocket

Our structure suggests that activation of Piezo1 may involve concerted movements of the inner helix, outer helix, CTD, anchor domain, latch and beam domains. Interdomain contacts that are likely to govern gating movements allosterically are shown in Fig. 4. The conserved anchor domain is poised to have a prominent involvement in gating through its interactions with the inner helix and CTD (Fig. 4b, c). In particular, anchor domain residue E2133 and R2482 of the adjacent inner helix are probably engaged in an electrostatic interaction. In previous studies, mutations at E2133 affected single-channel conductance and ion selectivity, and sensitivity to the pore blocker ruthenium red<sup>34</sup>. The equivalent mutation to R2482H in human PIEZO1 results in slower inactivation kinetics and is associated with dehydrated hereditary stomatocytosis<sup>10,12</sup>. In the context of the present structure, these data implicate the anchor domain–inner helix interaction in regulating gating and pore properties of Piezo1. The cytosolic membrane-lining helix of the anchor domain forms several contacts with the CTD (Fig. 4c), including potential electrostatic interaction(s) between R2169 and E2495/E2496, which are adjacent to pore-facing residues M2493 and F2494 (Fig. 3e). This interaction provides a possible explanation for why mutation of E2495 or E2496 affected the ion conduction properties of Piezo1<sup>28</sup>. Overall, the proximity of the anchor domain membrane-lining helix to the cytosolic neck of the permeation pathway suggests that its movement would be strongly coupled to channel gating.

We observe a robust lipid-shaped density in an apparent ligand-binding pocket formed by the anchor domain on one side and Piezo repeat A on the other (Fig. 4d). Two conserved arginine residues (R2035 and

R2135) project into the pocket, positioned to stabilize a negatively charged species. Notably, mutation of R2135 to alanine rendered Piezo1 non-functional<sup>34</sup>, suggesting that this ligand-binding pocket allosterically supports channel activity, and may therefore be a target for amphiphiles and other compounds aimed at modulating Piezo function. In addition, we note the presence of a separate density, potentially representing a lipid headgroup, that is sandwiched between Piezo repeats B and C (Extended Data Fig. 6e, f).

On the cytosolic side, the CTD interacts with the latch and beam (Fig. 4e). Latch residues Y1412, L1414 and F1415 protrude into the surface of the CTD, making contacts with K2528, F2531, E2537 and W2542 (Fig. 4e). Towards the C-terminal end of the beam, a series of basic and polar residues (R1351, R1353, Q1356 and R1360) face acidic CTD residues (D2509, E2518, E2520 and E2524). These electrostatic interactions probably promote allosteric coupling between the beam and CTD. Notably, the equivalent mutation to R1353P, which would presumably break or kink the helical beam at this position, is found in human patients with dehydrated hereditary stomatocytosis and results in delayed inactivation kinetics<sup>10</sup>. Thus, the distal beam end may be a structural determinant of gating behaviour, possibly through its interactions with the CTD.

### Concluding remarks

The Piezo1 structure described here represents the first, to our knowledge, high-resolution view of this functionally and structurally novel class of ion channel. Importantly, most known human PIEZO1 and PIEZO2 GOF disease mutants<sup>35,36</sup> can be mapped onto the structure, which indicates that our model encompasses many of the functionally important domains, and moreover, allows a structural interpretation of disease-causing mechanisms (Fig. 5a).

A central question in the study of Piezo channels is how membrane tension results in channel activation. A recent study probing for mechanosensitive domains in Piezo1<sup>37</sup> implicated regions as disparate as the N terminus (which probably resides towards the outer ‘tip’ of the propeller blade) and the central extracellular cap. Thus, mechanical activation is likely to involve movements of various domains spanning the entirety of the protein complex. Our structure clarifies the features that contribute to this process (Fig. 5b, c). The arrayed Piezo repeats potentially induce a remarkable degree of local membrane deformation, conceivably through their amphipathic helices. Although free energy calculations<sup>38</sup> have suggested that the energetic cost of local membrane deformation plays a key role in the mechanosensitivity of MscS<sup>25</sup> and TRAAK<sup>23</sup> channels, its contribution to Piezo structure and function in membrane bilayers will require further study. Nonetheless, our results allow us to speculate that membrane-tension-induced conformational changes of the Piezo repeats are transmitted through the beam and/or anchor domains to the inner helix and CTD, which in turn determine the activation state of the channel. The nature of these conformational transitions remains unclear, but the present structure of a closed state will guide further investigations of the process of Piezo mechanical activation.

**Online Content** Methods, along with any additional Extended Data display items and Source Data, are available in the online version of the paper; references unique to these sections appear only in the online paper.

Received 7 September; accepted 14 December 2017.

Published online 20 December 2017.

1. Ranade, S. S., Syeda, R. & Patapoutian, A. Mechanically activated ion channels. *Neuron* **87**, 1162–1179 (2015).
2. Coste, B. *et al.* Piezo1 and Piezo2 are essential components of distinct mechanically activated cation channels. *Science* **330**, 55–60 (2010).
3. Coste, B. *et al.* Piezo proteins are pore-forming subunits of mechanically activated channels. *Nature* **483**, 176–181 (2012).
4. Ranade, S. S. *et al.* Piezo2 is the major transducer of mechanical forces for touch sensation in mice. *Nature* **516**, 121–125 (2014).
5. Woo, S. H. *et al.* Piezo2 is the principal mechanotransduction channel for proprioception. *Nat. Neurosci.* **18**, 1756–1762 (2015).

6. Kim, S. E., Coste, B., Chadha, A., Cook, B. & Patapoutian, A. The role of *Drosophila* Piezo in mechanical nociception. *Nature* **483**, 209–212 (2012).
7. Li, J. *et al.* Piezo1 integration of vascular architecture with physiological force. *Nature* **515**, 279–282 (2014).
8. Nonomura, K. *et al.* Piezo2 senses airway stretch and mediates lung inflation-induced apnoea. *Nature* **541**, 176–181 (2017).
9. Zarychanski, R. *et al.* Mutations in the mechanotransduction protein PIEZO1 are associated with hereditary xerocytosis. *Blood* **120**, 1908–1915 (2012).
10. Albuissou, J. *et al.* Dehydrated hereditary stomatocytosis linked to gain-of-function mutations in mechanically activated PIEZO1 ion channels. *Nat. Commun.* **4**, 1884 (2013).
11. Andolfo, I. *et al.* Multiple clinical forms of dehydrated hereditary stomatocytosis arise from mutations in *PIEZO1*. *Blood* **121**, 3925–3935 (2013).
12. Bae, C., Gnanasambandam, R., Nicolai, C., Sachs, F. & Gottlieb, P. A. Xerocytosis is caused by mutations that alter the kinetics of the mechanosensitive channel PIEZO1. *Proc. Natl Acad. Sci. USA* **110**, E1162–E1168 (2013).
13. Coste, B. *et al.* Gain-of-function mutations in the mechanically activated ion channel PIEZO2 cause a subtype of Distal Arthrogyposis. *Proc. Natl Acad. Sci. USA* **110**, 4667–4672 (2013).
14. Lukacs, V. *et al.* Impaired PIEZO1 function in patients with a novel autosomal recessive congenital lymphatic dysplasia. *Nat. Commun.* **6**, 8329 (2015).
15. Chesler, A. T. *et al.* The role of PIEZO2 in human mechanosensation. *N. Engl. J. Med.* **375**, 1355–1364 (2016).
16. Mahmud, A. A. *et al.* Loss of the proprioception and touch sensation channel PIEZO2 in siblings with a progressive form of contractures. *Clin. Genet.* **91**, 470–475 (2017).
17. Haliloglu, G. *et al.* Recessive *PIEZO2* stop mutation causes distal arthrogyposis with distal muscle weakness, scoliosis and proprioception defects. *J. Hum. Genet.* **62**, 497–501 (2017).
18. Syeda, R. *et al.* Piezo1 channels are inherently mechanosensitive. *Cell Reports* **17**, 1739–1746 (2016).
19. Lewis, A. H. & Grandl, J. Mechanical sensitivity of Piezo1 ion channels can be tuned by cellular membrane tension. *eLife* **4**, e12088 (2015).
20. Cox, C. D. *et al.* Removal of the mechanoprotective influence of the cytoskeleton reveals PIEZO1 is gated by bilayer tension. *Nat. Commun.* **7**, 10366 (2016).
21. Kamajaya, A., Kaiser, J. T., Lee, J., Reid, M. & Rees, D. C. The structure of a conserved Piezo channel domain reveals a topologically distinct  $\beta$  sandwich fold. *Structure* **22**, 1520–1527 (2014).
22. Ge, J. *et al.* Architecture of the mammalian mechanosensitive Piezo1 channel. *Nature* **527**, 64–69 (2015).
23. Brohawn, S. G., Campbell, E. B. & MacKinnon, R. Physical mechanism for gating and mechanosensitivity of the human TRAAK K<sup>+</sup> channel. *Nature* **516**, 126–130 (2014).
24. Pliotas, C. *et al.* The role of lipids in mechanosensation. *Nat. Struct. Mol. Biol.* **22**, 991–998 (2015).
25. Phillips, R., Ursell, T., Wiggins, P. & Sens, P. Emerging roles for lipids in shaping membrane-protein function. *Nature* **459**, 379–385 (2009).
26. Jasti, J., Furukawa, H., Gonzales, E. B. & Gouaux, E. Structure of acid-sensing ion channel 1 at 1.9 Å resolution and low pH. *Nature* **449**, 316–323 (2007).
27. Kawate, T., Michel, J. C., Birdsong, W. T. & Gouaux, E. Crystal structure of the ATP-gated P2X<sub>4</sub> ion channel in the closed state. *Nature* **460**, 592–598 (2009).
28. Zhao, Q. *et al.* Ion permeation and mechanotransduction mechanisms of mechanosensitive Piezo channels. *Neuron* **89**, 1248–1263 (2016).
29. Long, S. B., Campbell, E. B. & MacKinnon, R. Crystal structure of a mammalian voltage-dependent Shaker family K<sup>+</sup> channel. *Science* **309**, 897–903 (2005).
30. Liao, M., Cao, E., Julius, D. & Cheng, Y. Structure of the TRPV1 ion channel determined by electron cryo-microscopy. *Nature* **504**, 107–112 (2013).
31. Coste, B. *et al.* Piezo1 ion channel pore properties are dictated by C-terminal region. *Nat. Commun.* **6**, 7223 (2015).
32. Drin, G. & Antonny, B. Amphipathic helices and membrane curvature. *FEBS Lett.* **584**, 1840–1847 (2010).
33. Bavi, N. *et al.* The role of MscL. Amphipathic N terminus indicates a blueprint for bilayer-mediated gating of mechanosensitive channels. *Nat. Commun.* **7**, 11984 (2016).
34. Mansoor, S. E. *et al.* X-ray structures define human P2X<sub>3</sub> receptor gating cycle and antagonist action. *Nature* **538**, 66–71 (2016).
35. Wu, J., Lewis, A. H. & Grandl, J. Touch, tension, and transduction - the function and regulation of Piezo ion channels. *Trends Biochem. Sci.* **42**, 57–71 (2017).
36. Glogowska, E. *et al.* Novel mechanisms of PIEZO1 dysfunction in hereditary xerocytosis. *Blood* **130**, 1845–1856 (2017).
37. Wu, J., Goyal, R. & Grandl, J. Localized force application reveals mechanically sensitive domains of Piezo1. *Nat. Commun.* **7**, 12939 (2016).
38. Ursell, T., Kondev, J., Reeves, D., Wiggins, P. & Phillips, R. in *Mechanosensitive Ion Channels* Vol. 1 (eds Kamkin, A. & Kiseleva, I.) 37–70 (Springer, 2008).

**Supplementary Information** is available in the online version of the paper.

**Acknowledgements** We thank H. Turner and G. Ozorowski for assistance with electron microscopy data collection. We acknowledge early efforts to characterize Piezo1 using electron microscopy by E. Wilson-Kubalek and R. Milligan, and S. Kakuda for screening purification conditions. We thank A. Sobolevsky for critical reading of the manuscript, and members of the Ward and Patapoutian laboratories for discussion. This work was supported by a Ray Thomas Edwards Foundation grant to A.B.W. and National Institutes of Health (NIH) grants NS083174 and DE022358 to A.P. Computational analyses were performed using shared instrumentation funded by NIH 1-S10OD021634. A.P. is an investigator of the Howard Hughes Medical Institute. This is manuscript 29582 from The Scripps Research Institute.

**Author Contributions** K.S. prepared electron microscopy samples, collected and processed electron microscopy data, built the structural model and conducted fluorescence-detection size-exclusion chromatography analysis. S.E.M. carried out electrophysiological experiments and data analysis. J.M.K. developed sample preparation protocols. T.W. carried out immunostaining experiments. A.P. and A.B.W. supervised the project. K.S. drafted the manuscript, which was edited by A.P. and A.B.W. with input from all authors.

**Author Information** Reprints and permissions information is available at [www.nature.com/reprints](http://www.nature.com/reprints). The authors declare no competing financial interests. Readers are welcome to comment on the online version of the paper. Publisher's note: Springer Nature remains neutral with regard to jurisdictional claims in published maps and institutional affiliations. Correspondence and requests for materials should be addressed to A.P. ([ardem@scripps.edu](mailto:ardem@scripps.edu)) or A.B.W. ([andrew@scripps.edu](mailto:andrew@scripps.edu)).

## METHODS

No statistical methods were used to predetermine sample size. The experiments were not randomized and investigators were not blinded to allocation during experiments and outcome assessment.

**Sample preparation.** Protocols to purify mouse Piezo1 were adapted from a previous study<sup>22</sup> with modifications. Suspension-adapted HEK293F cells (purchased and authenticated from ATCC, tested negative for mycoplasma) were grown at 37 °C to a cell density of approximately 1.5 million per ml and transfected with a pcDNA3.1-IRES-GFP plasmid<sup>22</sup> containing mouse Piezo1 (Uniprot KB accession number E2JF22) fused to a Prescission protease cleavage site (LEVLFQGP) followed by a glutathione *S*-transferase GST coding sequence (this plasmid was a gift from B. Xiao). For transfection, DNA (300 µg) and polyethylenimine (900 µg) were added per litre of HEK cells. Sodium butyrate (4 mM) was added to the cells 12–24 h after transfection. Approximately 48 h after transfection, cells were collected and resuspended in buffer containing 25 mM PIPES pH 7.2, 150 mM NaCl, 1% CHAPS, 0.5% soy phosphatidylcholine, 0.1% C<sub>12</sub>E<sub>9</sub>, 2 mM dithiothreitol (DTT), and cComplete protease inhibitor cocktail (Roche). The lysate was stirred for 1 h at 4 °C, clarified by centrifugation, and incubated with Glutathione Sepharose 4B resin (GE Healthcare) for 3 h. The resin was washed extensively with buffer A (25 mM HEPES pH 8.0, 150 mM NaCl, 100 µM glyco-diosgenin, 2 mM DTT). Prescission protease was added to a ~30% slurry of resin in buffer A at a ratio of approximately 100 µg per ml resin and incubated at 4 °C overnight. The flow-through was concentrated and subjected to size-exclusion chromatography on a Superose 6 increase column equilibrated to buffer A. The peak corresponding to Piezo1 trimer was collected and concentrated to ~5 mg ml<sup>-1</sup>. Protein (3.5 µl) was applied to a freshly plasma cleaned UltraAuFoil R1.2/1.3 grid, blotted for 3.5 s with a blot force of 0, and plunge-frozen in liquid ethane using a Vitrobot Mark IV (FEI). **Cryo-EM data collection.** An initial dataset of mouse Piezo1 was collected in a Talos Arctica electron microscope (FEI) equipped with a K2 direct detector camera (Gatan) operated at 200 kV and having a nominal pixel size of 1.15 Å. Subsequent data were collected on a Titan Krios electron microscope (FEI) equipped with a K2 direct detector camera (Gatan) operated at 300 kV and having a nominal pixel size of 1.03 Å. Micrographs were automatically collected using Legion software<sup>39</sup>. The total accumulated dose was ~60 e<sup>-</sup> Å<sup>-2</sup> and the target defocus range was 0.8–2.2 µm. Micrograph movie frames were dose-weighted and aligned using MotionCor2<sup>40</sup>. CTF values were estimated using Gctf<sup>41</sup>.

**Image processing.** Template-based particle picking, 2D and 3D classification, and 3D refinements were carried out in Relion 2.0<sup>42</sup>. Unwanted particle picks due to ice contaminations or the grid hole edges were removed using EM Hole Punch<sup>43</sup>. An initial set of 527 micrographs was collected on the Talos Arctica microscope, from which approximately 96,000 particle images were extracted. After reference-free 2D classification and 3D classification using the published medium-resolution Piezo1 reconstruction<sup>22</sup> as an initial reference (low-pass filtered to 60 Å), a ~26,000 particle subset was identified that refined to a ~5 Å resolution reconstruction with C3 symmetry applied.

Two separate data collection sessions were conducted on the Titan Krios microscope. 1,978 micrographs were collected in session 1, yielding approximately 281,000 particles. This particle stack was subjected to 2D classification to remove classes not displaying well-defined features of the Piezo1 trimer, resulting in 266,000 particles. In session 2, 1,086 micrographs were collected, yielding approximately 144,000 particles from which 112,000 particles were chosen after 2D classification. The post-2D classification particle stacks from sessions 1 and 2 were combined into a stack with approximately 378,000 particles. This stack was subjected to 3D classification requesting three classes, using a 60 Å low-pass-filtered map of mouse Piezo1 generated from the Talos Arctica dataset as an initial reference. The best class contained 106,000 particles, which were subjected to a round of 3D classification without alignment requesting six classes. The most populated class from this round of refinement contained 73,000 particles. Auto-refinement of these particles with and without C3 symmetry imposed resulted in reconstructions at 3.9 and 4.5 Å resolution, respectively. C3 symmetry imposed refinement with a soft mask around the Piezo1 core (cap, inner and outer helices, anchor, CTD, Piezo repeats A–C, latch and beam domains) requesting local searches resulted in a 3.8 Å resolution map with improved features.

Inspection of the asymmetrically refined map indicated a progressive break of symmetry towards the blade periphery (Extended Data Fig. 3a). To resolve the peripheral regions of the blade better, *relion\_particle\_symmetry\_expand* was used to enlarge the particle stack threefold artificially, and add 120° or 240° to the first Euler angle determined in the initial C1 refinement. Alignment-free 3D classification of these approximately 220,000 ‘expanded’ particles requesting six classes with a soft mask around a single blade yielded two highly populated classes containing approximately 102,000 (blade class 1) and 74,000 expanded particles (blade class 2) with distinct blade conformations. Refinement with a

soft mask around a single blade and the most symmetric parts of the molecule (cap, anchor, Piezo repeat A, inner and outer helices) and requesting local angular searches resulted in reconstructions at 4.1 (blade class 1) and 4.5 Å (blade class 2) resolution, respectively.

**Model building and refinement.** The 3.8 Å resolution map of the Piezo1 core sharpened with a *B*-factor of –118 automatically determined using *relion\_post-process* was primarily used for model building and refinement. Initially, the crystal structure of the extracellular cap domain<sup>22</sup> (PDB code 4RAX) was docked as a rigid body, and a poly-alanine model was fitted into the rest of the Piezo1 core. Rough sequence assignment was ascertained from the position of the docked cap domain, as well as transmembrane topology prediction and previous immunostaining and mass spectrometry data<sup>34</sup> demonstrating the positions of extracellular loops and intracellular phosphorylation sites, respectively. We were able to model amino acids for 14 out of the 26 transmembrane helices observed in our electron microscopy maps. We note here that the previous membrane topology analysis<sup>34</sup> approximates the presence of 21 transmembrane helices in addition to the 14 we have modelled. The N and C termini of the channel are intracellular<sup>34</sup>, necessitating an even number of transmembrane helix segments. This would suggest a putative total of 34 or 36 transmembrane helices, and up to 8 Piezo repeats per protomer. Nonetheless, additional studies are needed to clarify the exact membrane topology of Piezo proteins.

Precise sequence registry assignment was determined by locating bulky Phe, Arg, Tyr, and Trp side chains, as well as the absence of side-chain density for Gly. Side-chain densities were not well resolved for many Asp and Glu side chains, probably owing to radiation damage<sup>44</sup>. Some portions of the beam and Piezo repeats B and C were built using the blade class 1 map (sharpened to an automatically determined *B*-factor of –152), then symmetrized three-fold to fit into the C3 symmetry core map. Iterative manual model building and automatic refinement were carried out in Coot<sup>45</sup>, and *Phenix.real\_space\_refine*<sup>46</sup>, respectively. Final structural refinement was carried out in the C3 symmetry core map, with strong restraints applied to portions built using the blade class 1 map, as well as non-crystallographic symmetry restraints for the entire model. Model geometry and fit to map were validated using MolProbity<sup>47</sup> and EMRinger<sup>48</sup>. Electrostatic potential surfaces were calculated using APBS<sup>49</sup>. Structural figures were made in PyMOL<sup>50</sup> or UCSF Chimera<sup>51</sup>.

**Generation of mutants.** Mouse Piezo1 mutants M2493A, F2494A and double mutant M2493A/F2494A were generated using QuickChange II XL site-directed mutagenesis kit according to the manufacturer's instruction and confirmed by full-length DNA sequencing. All mouse Piezo1 constructs were inserted into an IRES-GFP pcDNA3.1 vector.

**Cell culture and transfections.** Wild-type and mutant mouse Piezo1 were transfected and tested in Piezo1-knockout (P1KO) HEK293T cells. HEK293T-P1KO cells were generated using CRISPR-Cas9 nuclease genome editing technique as described previously<sup>14</sup> and not tested for mycoplasma contamination nor further authenticated. Cells were grown in DMEM containing 4.5 mg ml<sup>-1</sup> glucose, 10% fetal bovine serum, 50 U ml<sup>-1</sup> penicillin and 50 µg ml<sup>-1</sup> streptomycin. Cells were plated onto 12-mm round glass poly-D-lysine coated coverslips placed in 24-well plates and transfected using Lipofectamine 2000 (Invitrogen) according to the manufacturer's instruction. All plasmids were transfected at a concentration of 600 ng ml<sup>-1</sup>. Cells were recorded from 24 to 36 h after transfection.

**Electrophysiology.** Patch-clamp experiments were performed in standard whole-cell or cell-attached mode using Axopatch 200B amplifier (Axon Instruments). Macroscopic currents were filtered at 2 kHz and sampled at 20 kHz. Leak currents before mechanical stimulations were subtracted off-line from the current traces. Voltages were not corrected for a liquid junction potential except for ion selectivity experiments. Liquid junction potential was calculated using Clampex 10.3 software. All experiments were done at room temperature.

**Mechanical stimulation:** For whole-cell recordings, mechanical stimulation was achieved using a fire-polished glass pipette (tip diameter 3–4 µm) positioned at an angle of 80° relative to the cell being recorded. Downward displacement of the probe towards the cell was driven by Clampex-controlled piezoelectric crystal microstage (E625 LVPZT Controller/Amplifier; Physik Instrumente). The probe had a velocity of 1 µm ms<sup>-1</sup> during the ramp phase of the command for forward movement and the stimulus was applied for 150 or 300 ms. To assess the mechanical sensitivity of a cell, a series of mechanical steps in 0.5 or 1 µm increments was applied every 20 s. For *I–V* relationship recordings, voltage steps were applied 700 ms before mechanical stimulation (150 ms) from a holding potential of –60 mV. Voltage steps were given from –80 mV to +80 in 20 mV increments.

Stretch-activated currents were recorded in the cell-attached patch-clamp configuration. Membrane patches were stimulated with a 5 s prepulse duration of +5 or 0 mm Hg followed by 500 ms negative pressure pulses through the

recording electrode using Clampex-controlled pressure clamp HSPC-1 device (ALA-scientific)<sup>19</sup>. Because the single-channel amplitude is independent of the pressure intensity, the most optimal pressure stimulation was used to elicit responses that allowed single-channel amplitude measurements. These stimulation values were largely dependent on the number of channels in a given patch of the recording cell. Single-channel amplitude at a given potential was measured from trace histograms of 5–10 repeated recordings. Histograms were fitted with Gaussian equations using Clampfit 10.3 software. Single-channel slope conductance for each individual cell was calculated from linear regression curve fit to single-channel  $I-V$  plots.

**Solutions:** For whole-cell patch-clamp recordings, recording electrodes had a resistance of 2–3 M $\Omega$  when filled with internal solution composed of (in mM) 133 CsCl, 1 CaCl<sub>2</sub>, 1 MgCl<sub>2</sub>, 5 EGTA, 10 HEPES (pH 7.3 with CsOH), 4 MgATP and 0.4 Na<sub>2</sub>GTP. The extracellular solution was composed of (in mM) 133 NaCl, 3 KCl, 2.5 CaCl<sub>2</sub>, 1 MgCl<sub>2</sub>, 10 HEPES (pH 7.3 with NaOH) and 10 glucose. For ion-selectivity experiments, internal solution used was (in mM) 150 CsCl, 10 HEPES (pH 7.3 with CsOH) and extracellular solution consisted of (in mM) 100 CaCl<sub>2</sub> and 10 HEPES (pH 7.3 with CsOH).

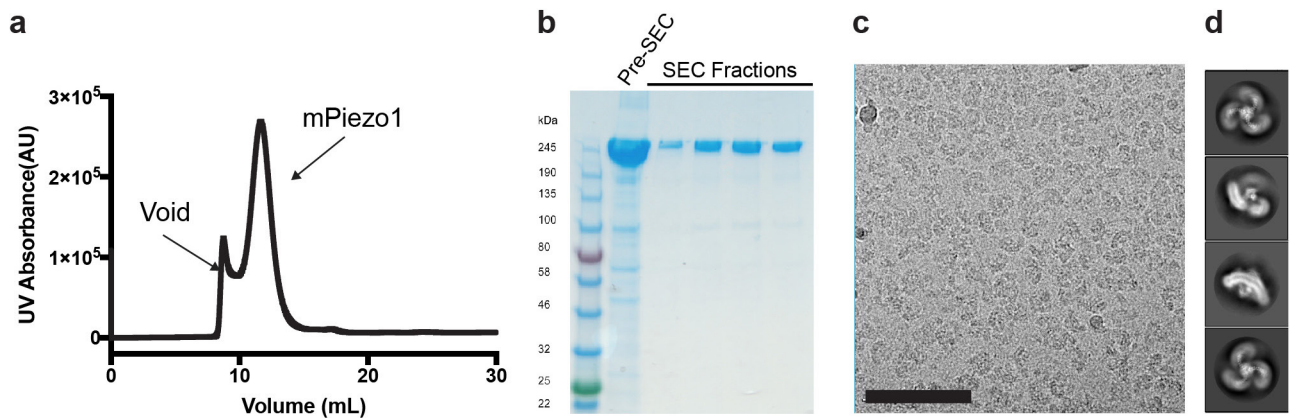
For cell-attached patch-clamp recordings, external solution used to zero the membrane potential consisted of (in mM) 140 KCl, 1 MgCl<sub>2</sub>, 10 glucose and 10 HEPES (pH 7.3 with KOH). Recording pipettes were of 1–3 M $\Omega$  resistance when filled with standard solution composed of (in mM) 130 mM NaCl, 5 KCl, 1 CaCl<sub>2</sub>, 1 MgCl<sub>2</sub>, 10 TEA-Cl and 10 HEPES (pH 7.3 with NaOH).

**Surface immunostaining.** Surface immunostaining of Piezo1 was carried out as described previously<sup>34</sup>, with slight modifications. In brief, pcDNA3.1 IRES-GFP vector encoding wild-type or mutant Piezo1 constructs containing the Myc tag (EQKLISEEDL) inserted at a previously determined extracellular amino acid position 897<sup>34</sup> were expressed in HEK293T-P1KO cells on poly-D-lysine-treated glass coverslips. Two days after transfection, labelling of non-permeabilized cells was carried out by incubating the cells with 9E11 anti-Myc antibody (1:50; Santa Cruz Biotechnology). After six washes with warm medium, cells were incubated with secondary antibodies conjugated to Alexa Fluor 568 (1:200; Life Technologies) for 10 min at room temperature. Cells were washed six times with warm medium and once with PBS, and then fixed with 4% paraformaldehyde (PFA) in PBS for 30 min. For permeabilization, cells were fixed with 4% PFA for 10 min and then treated with 0.3% Triton X-100 and blocked with 10% normal goat serum in PBS before incubation with antibodies (primary: 1:200 for 2 h, secondary: 1:400 for 1 h, in block solution). Cells were imaged with a Nikon C2 confocal microscope with 40 $\times$  oil immersion objective by illumination with the 543 nm laser. The live labelling and permeabilized staining were repeated in three separate experiments to confirm results.

**Fluorescence detection size-exclusion chromatography.** Suspension-adapted HEK293F cells were transfected with pcDNA3.1 vector containing wild-type Piezo1 or the M2493A/F2494A double mutant fused to tdTomato at the C terminus. Then, 48 h after transfection, 1 ml of the culture was pelleted and resuspended in 200  $\mu$ l of buffer containing 25 mM HEPES pH 8.0, 150 mM NaCl, 1% CHAPS, 0.5% soy phosphatidylcholine, 1 mM PMSE, 2  $\mu$ M pepstatin A, 2  $\mu$ g ml<sup>-1</sup> aprotinin, 2  $\mu$ g ml<sup>-1</sup> leupeptin. One-hundred microlitres of clarified supernatant was injected into a Superose 6 increase column in line with a fluorimeter tracking tdTomato fluorescence (excitation at 554 nm, emission at 581 nm).

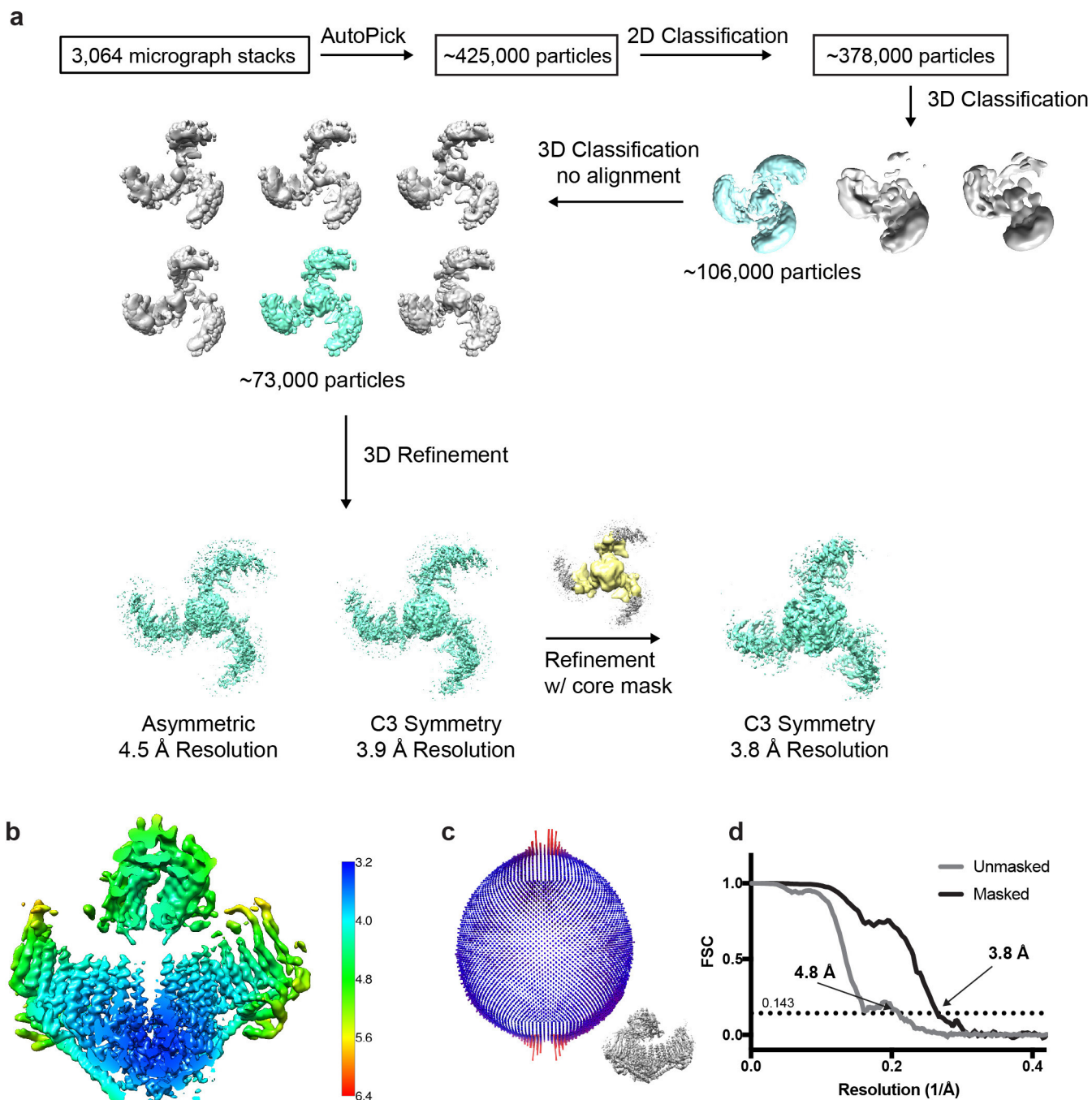
**Data availability.** Electron microscopy maps have been deposited into the Electron Microscopy Data Bank (EMDB) under accession code EMD-7128. A structural model has been deposited to Protein Data Bank (PDB) under accession code 6BPZ. All other data can be obtained from the corresponding authors upon reasonable request.

39. Suloway, C. *et al.* Automated molecular microscopy: the new Legion system. *J. Struct. Biol.* **151**, 41–60 (2005).
40. Zheng, S. Q. *et al.* MotionCor2: anisotropic correction of beam-induced motion for improved cryo-electron microscopy. *Nat. Methods* **14**, 331–332 (2017).
41. Zhang, K. Gctf: Real-time CTF determination and correction. *J. Struct. Biol.* **193**, 1–12 (2016).
42. Scheres, S. H. RELION: implementation of a Bayesian approach to cryo-EM structure determination. *J. Struct. Biol.* **180**, 519–530 (2012).
43. Berndsen, Z., Bowman, C., Jang, H. & Ward, A. B. EMHP: An accurate automated hole masking algorithm for single-particle cryo-EM image processing. *Bioinformatics* **33**, 3823–3826 (2017).
44. Bartesaghi, A., Matthies, D., Banerjee, S., Merk, A. & Subramaniam, S. Structure of beta-galactosidase at 3.2-Å resolution obtained by cryo-electron microscopy. *Proc. Natl Acad. Sci. USA* **111**, 11709–11714 (2014).
45. Emsley, P., Lohkamp, B., Scott, W. G. & Cowtan, K. Features and development of Coot. *Acta Crystallogr. D* **66**, 486–501 (2010).
46. Adams, P. D. *et al.* PHENIX: a comprehensive Python-based system for macromolecular structure solution. *Acta Crystallogr. D* **66**, 213–221 (2010).
47. Chen, V. B. *et al.* MolProbity: all-atom structure validation for macromolecular crystallography. *Acta Crystallogr. D* **66**, 12–21 (2010).
48. Barad, B. A. *et al.* EMRinger: side chain directed model and map validation for 3D cryo-electron microscopy. *Nat. Methods* **12**, 943–946 (2015).
49. Unni, S. *et al.* Web servers and services for electrostatics calculations with APBS and PDB2PQR. *J. Comput. Chem.* **32**, 1488–1491 (2011).
50. The PyMOL Molecular Graphics System. Version 1.8 Schrödinger, LLC; <http://www.pymol.org/> (2015).
51. Pettersen, E. F. *et al.* UCSF Chimera—a visualization system for exploratory research and analysis. *J. Comput. Chem.* **25**, 1605–1612 (2004).



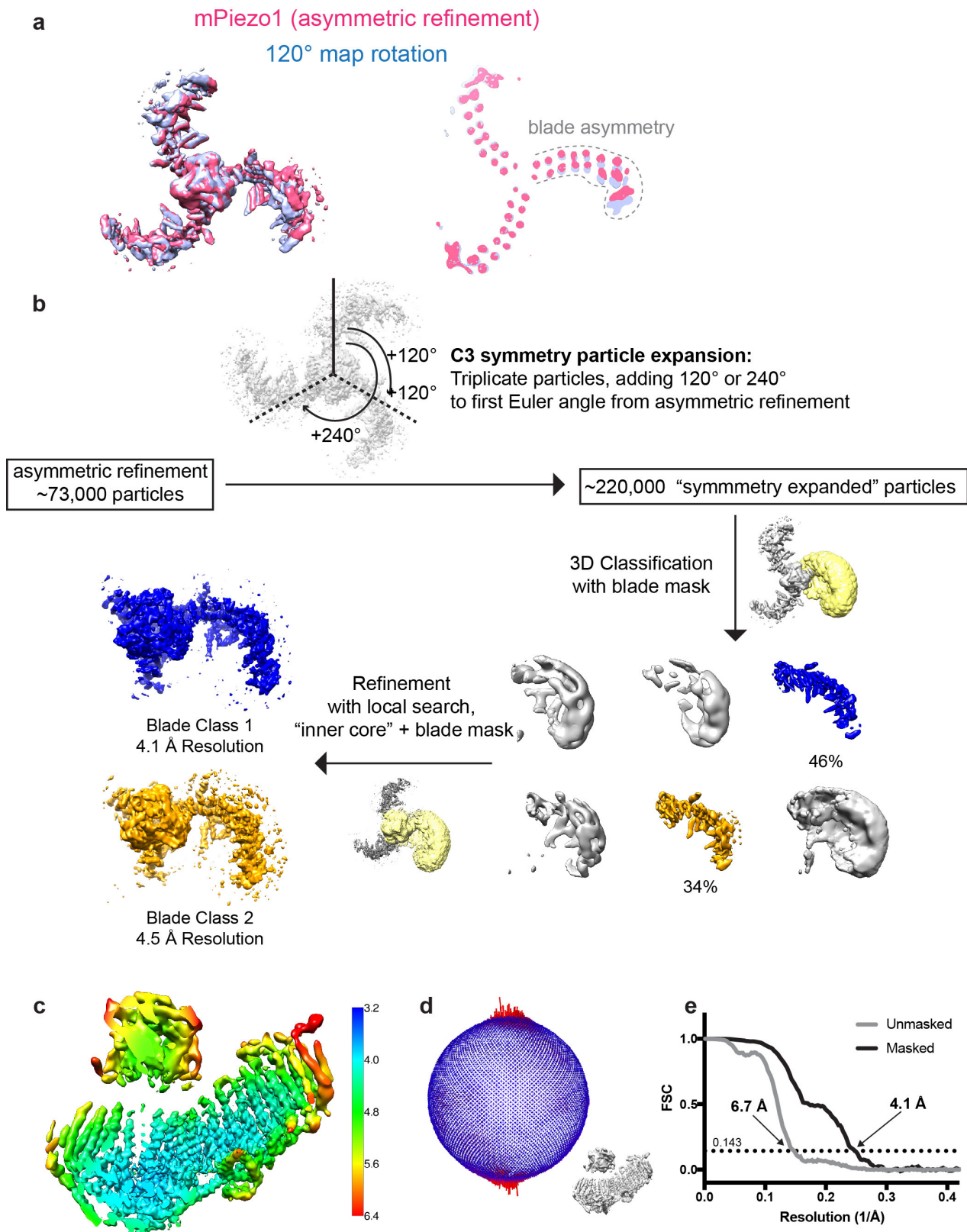
**Extended Data Figure 1 | Purification and electron microscopy analysis of Piezo1.** **a**, Preparative gel filtration chromatogram of mouse Piezo1 after affinity purification and proteolytic removal of the GST tag. **b**, SDS-PAGE analysis of Piezo1 following affinity purification (pre-SEC) and after subsequent size-exclusion chromatography (SEC) steps (SEC fractions).

Purifications of Piezo1 have been repeated more than three times with similar results. **c**, Aligned micrograph of purified Piezo1 embedded in a thin layer of vitrified ice. Scale bar, 100 nm. **d**, Representative 2D classes of Piezo1 showing different particle orientations.



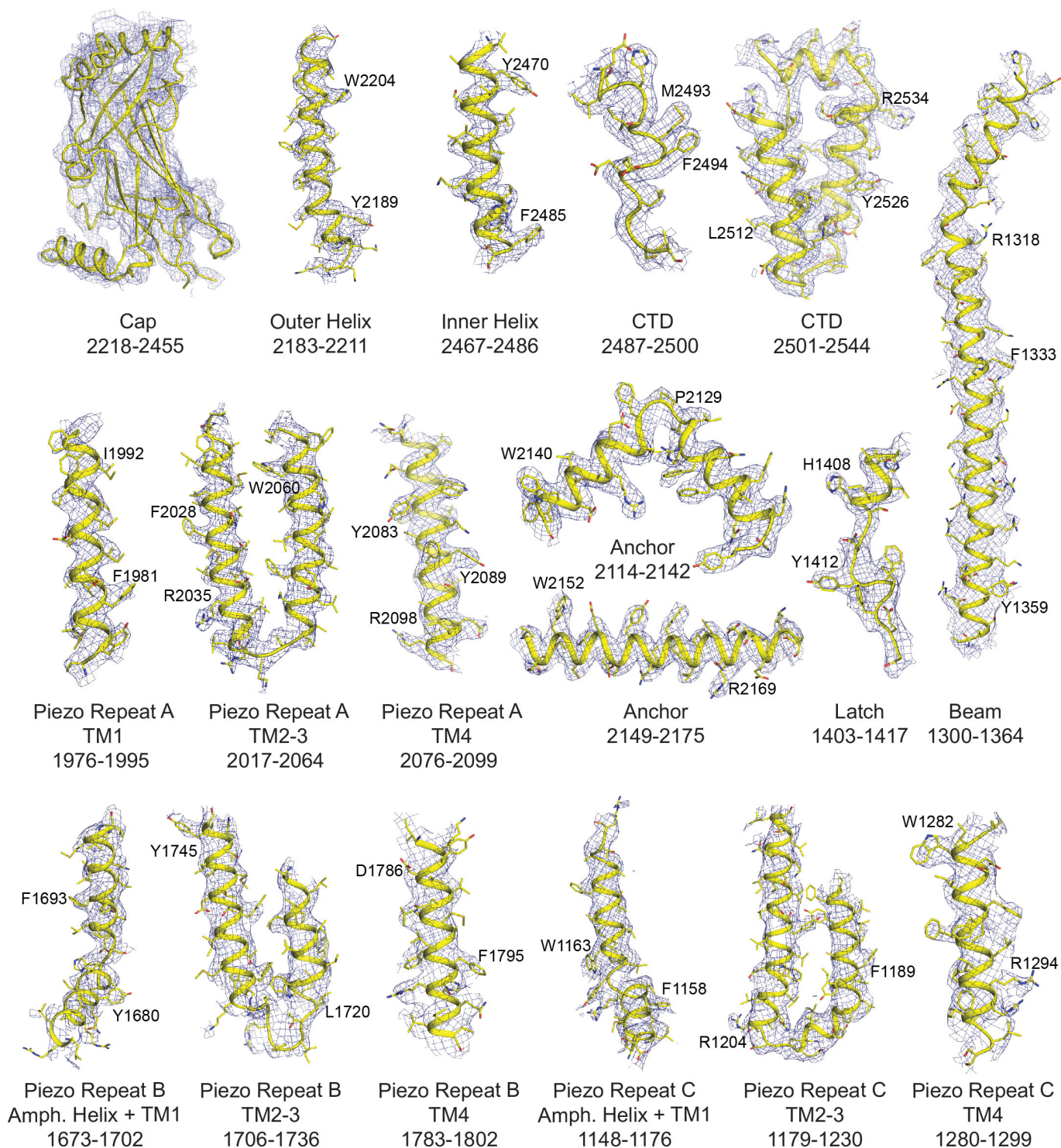
**Extended Data Figure 2 | Classification and refinement of Piezo1 core.**  
**a**, Data processing flow chart. **b**, Local resolution maps calculated by the *locres* program in RELION 2.0. Colour key for local resolution (in Å) is shown. **c**, Angular distributions of the particles after the final step of refinement in RELION. The radius of the sphere is proportional to the

number of particles with a given orientation. Only one-third of the sphere is shown due to applied C3 symmetry. **d**, FSC plots calculated using *relion\_postprocess* for unmasked maps and maps with a soft mask applied to remove the contribution of scattered detergent density.

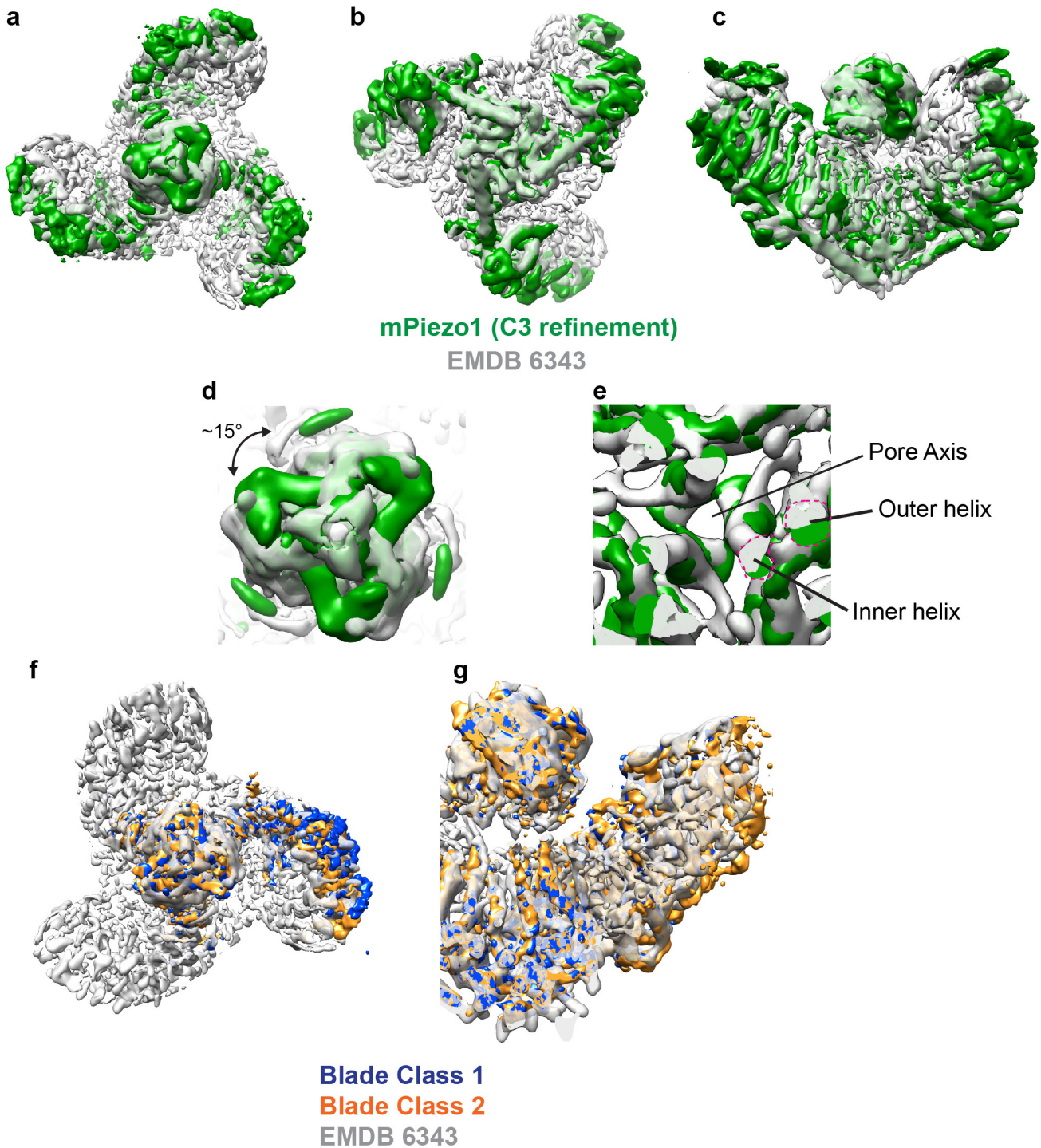


**Extended Data Figure 3 | Asymmetry of Piezo1 and blade-focused classification and refinement.** **a**, Duplicate unsharpened maps of Piezo1 refined without symmetry imposed, with the blue map rotated approximately 120° around the central axis of pseudosymmetry relative to the pink map, then superimposed with the ‘fit in map’ function of UCSF Chimera. The left panel shows top view, while the right panel shows a horizontal slice through the transmembrane region. **b**, Flow chart of propeller blade-focused classification and refinement procedure. **c**, Local

resolution maps calculated by the locres program in RELION 2.0. Colour key for local resolution (in Å) is shown and is the same as Extended Data Fig. 2b. **d**, Angular distributions of the particles after the final step of refinement in RELION. The radius of the sphere is proportional to the number of particles with a given orientation. **e**, FSC plots calculated using relion\_postprocess for unmasked maps and maps with a soft mask applied to remove the contribution of scattered detergent density.

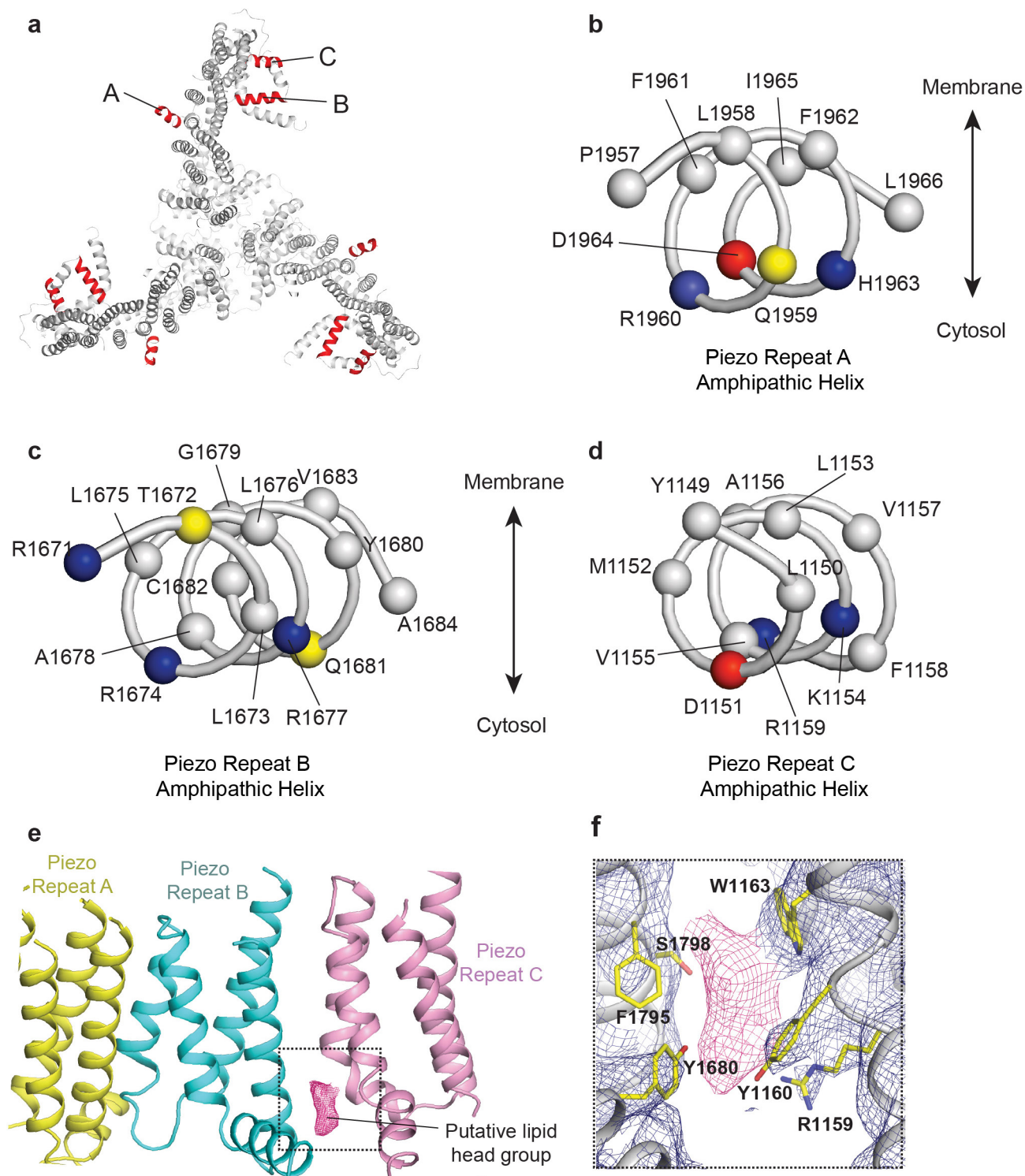


**Extended Data Figure 4 | Fit of molecular model to electron density.** Select regions of the molecular model are shown as yellow cartoon, with superimposed electron density as blue mesh. The density is derived from the C3-symmetry core masked map for the top two rows, and derived from blade class 1 for the bottom row.



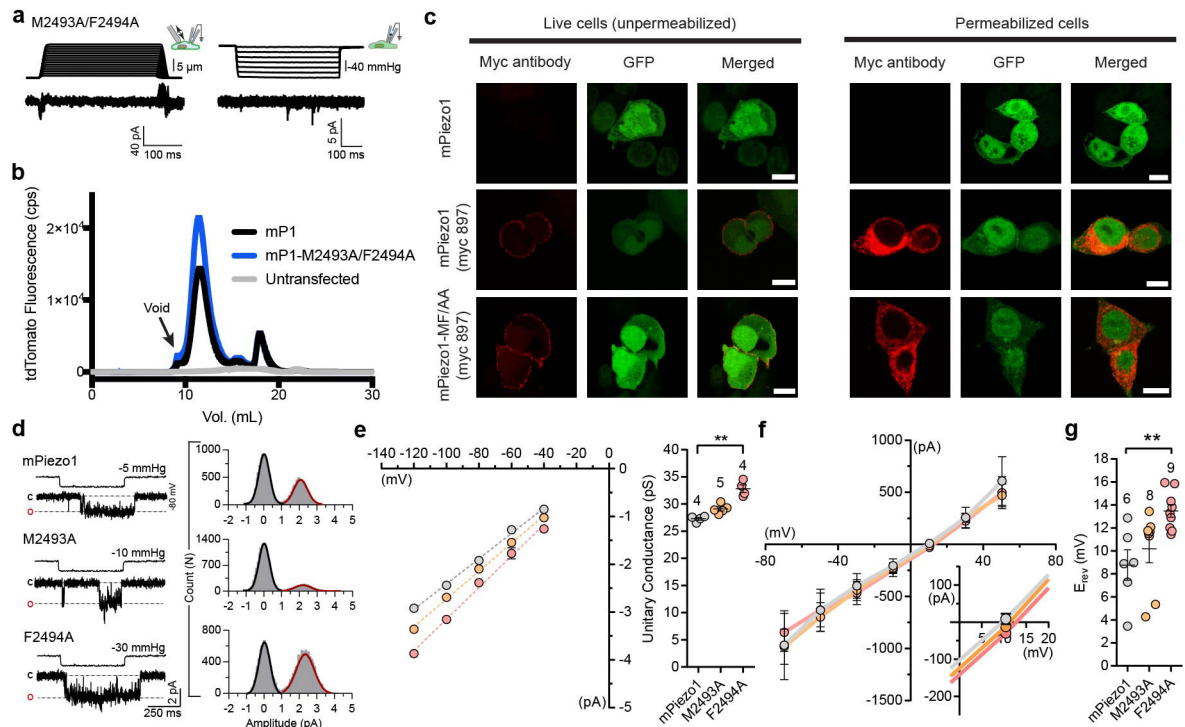
**Extended Data Figure 5 | Structural comparisons of current and previous (EMDB 6343) mouse Piezo1 structures.** For each panel, the 'fit in map' function of UCSF Chimera was used to align uncropped maps. In **a–e**, unsharpened map of C3 refinement is shown. **a–c**, Top (**a**), bottom (**b**) and side (**c**) views of current Piezo1 (green) and EMD accession EMD-6343 (grey) structurally aligned. **d**, Expanded top view of the cap domain to illustrate an approximately 15° rotation of the cap between the

two maps. **e**, Expanded sliced top view of pore-proximal transmembrane region. Subtle conformational rearrangements are present between the current and previous structures in the inner and outer helices. **f, g**, Top and side views of EMD accession EMD-6343 (grey), blade class 1 (blue), and blade class 2 (orange). The trajectories of the propeller blades are broadly similar across the maps in both the membrane-parallel and membrane-normal directions.



**Extended Data Figure 6 | Structural features of Piezo repeats.** **a**, Top view of Piezo1 depicted as cartoon, with amphipathic helices from Piezo repeats A, B and C shown in red. Extracellular cap domain is omitted for clarity. **b–d**, Ribbon models of amphipathic helices from Piezo repeat A (**b**), Piezo repeat B (**c**), and Piezo repeat C (**d**).  $C_{\alpha}$  positions are shown as spheres and hydrophobic amino acids are coloured grey, basic amino acids are coloured blue, acidic amino acids are coloured red, and polar uncharged amino acids are coloured yellow. **e**, Cartoon model of a portion

of the Piezo1 propeller blade, with Piezo repeats coloured separately. A strong density peak putatively representing a lipid head group is shown as a pink mesh. **f**, Expanded view of the putative lipid binding site sandwiched between Piezo repeats B and C (helices B4 and C1). Electron density (blue mesh) is superimposed onto the molecular model, and the putative lipid head group is shown as pink mesh. Side chains contributing to the binding pocket are shown as yellow sticks and labelled.



**Extended Data Figure 7 | Expression and functional properties of Piezo1 mutants.** **a**, HEK293T cells deficient in Piezo1 (P1KO) that express the Piezo1 double mutant M2493A/F2494A do not show discernible currents activated by indentation with blunt pipette (left) or stretch (right). **b**, Fluorescence-detection size-exclusion chromatography traces of untransfected HEK293F cells (grey) or cells expressing C-terminal tdTomato fusions of wild-type Piezo1 or double mutant M2493A/F2494A injected into Superose 6 increase column. Similar to the wild type, the double mutant displays a single dominant peak eluting shortly after void volume, indicating proper trimeric expression. Data are from one independent experiment. **c**, Representative images of Myc labelling in HEK293T-P1KO cells transfected with Piezo1-IRES-GFP (top), Piezo1-Myc-IRES-GFP (middle) or Piezo1(M2493A/F2494A)-Myc-IRES-GFP (bottom). GFP, green fluorescent protein. IRES, internal ribozyme entry site. Myc tags were inserted at position 897. Immunostaining was performed before (left) or after (right) cell permeabilization. Piezo1(M2493A/F2494A)-Myc is labelled at the surface in live cells similar to Piezo1-Myc, indicating that surface expression is preserved in the non-functional mutant. Scale bar, 10  $\mu\text{m}$ . Experiments were repeated three times with reproducible results. **d**, Left, representative traces of stretch-activated single channel currents recorded ( $-80$  mV) from HEK293T-

P1KO cells expressing wild-type, M2493A or F2494A Piezo1 channels (traces displayed after applying 1 kHz digital filter). The corresponding pressure stimulus used to elicit the response is illustrated above the current trace. For each condition, the amplitude histogram for the corresponding trace is depicted on the right. The Gaussian fit for the closed (black curve) and open (red curve) components is overlaid on the histograms. **e**, Left, average  $I-V$  relationship of stretch-activated single-channel currents from wild-type ( $n=4$ ), M2493A ( $n=5$ ) or F2494A ( $n=4$ ) Piezo1 channels. Amplitude was measured as a difference in Gaussian fits of full-trace histograms. Right, mean unitary conductance calculated from the slope of linear regression line fit to individual cells in each condition. **\*\*** $P < 0.01$ , one-way ANOVA with Dunn's comparison. **f**, Mean  $I-V$  relationship curves of mechanically activated currents recorded from wild-type ( $n=6$ ), M2493A ( $n=8$ ) or F2494A ( $n=9$ ) Piezo1 channels with 150 mM CsCl-based intracellular solution and 100 mM  $\text{CaCl}_2$ -based extracellular solution. Currents were elicited from  $-69.6$  to  $50.4$  mV ( $\Delta 20$  mV). Inset, expanded view of curves between 5 and 15 mV. Values are mean  $\pm$  s.e.m. **g**, Mean reversal potential from individual cells; Piezo1:  $8.8 \pm 1.3$  mV ( $n=6$ ), M2493A:  $10.2 \pm 1.2$  mV ( $n=8$ ) and F2494A:  $13.5 \pm 0.5$  mV ( $n=9$ ). **\*\*** $P = 0.0063$ , one-way ANOVA with Dunn's multiple comparison test.  $N$  denotes  $X$  individual cells.

Extended Data Table 1 | EM data collection, data processing, model refinement and validation

	mPiezo1 Core (EMDB-7128) (PDB 6BPZ)	mPiezo1 Blade Class 1 (EMDB-7128)
<b>Data collection and processing</b>		
Magnification	29,000	29,000
Voltage (kV)	300	300
Electron exposure ( $e^{-}/\text{\AA}^2$ )	60	60
Defocus range ( $\mu\text{m}$ )	0.8-2.2	0.8-2.2
Pixel size ( $\text{\AA}$ )	1.03	1.03
Symmetry imposed	C3	C1*
Initial particle images (no.)	425,103	425,103
Final particle images (no.)	72,627	102,289*
Map resolution ( $\text{\AA}$ )	3.8	4.1
FSC threshold	0.143	0.143
<b>Refinement</b>		
Map sharpening $B$ factor ( $\text{\AA}^2$ )	-118	-152
Model composition		
Protein residues	2700	
Ligands	0	
R.m.s. deviations		
Bond lengths ( $\text{\AA}$ )	0.01	
Bond angles ( $^\circ$ )	1.52	
Validation		
MolProbity score	1.68	
Clashscore	4.1	
EMRinger score	1.62	
	2.54 <sup>†</sup>	
Poor rotamers (%)	0.27	
Ramachandran plot		
Favored (%)	91.8	
Allowed (%)	8.0	
Disallowed (%)	0.2	

\*Particles are C3-symmetry expanded (triplicated, adding 120° or 240° to first Euler angle from unmasked asymmetric refinement, then classified with mask around single blade before refinement).

<sup>†</sup>EMRinger score calculated for 'inner core', which includes Piezo repeat A, the anchor, inner helix, outer helix, CTD and latch domains.

Extended Data Table 2 | Mechanically activated current properties of Piezo1 constructs

Construct	Whole-cell/Poke				Cell-attached/Stretch				
	I <sub>max</sub> (pA)	Threshold ( $\mu$ m)	Tau Inactivation (ms)	E <sub>rev</sub> (mV)	I <sub>max</sub> (pA)	P <sub>50</sub> (mmHg)	Tau Inactivation* (ms)	%SS*	Unitary Conductance (pS)
mPiezo1	2398 ± 728 (7)	3.8 ± 0.31 (7)	13 ± 1 (7)	8.7 ± 1.3 (6)	77 ± 18 (6)	30.7 ± 5.5 (5)	37.6 ± 6 (6)	10.4 ± 1.8 (6)	27.3 ± 0.3 (4)
M2493A	3120 ± 607 (8)	3.6 ± 0.3 (8)	19.6 ± 1.2 (8)	10.2 ± 1.2 (8)	232 ± 73 (7)	47.2 ± 8.7 (7)	68.6 ± 6.3 (7)	11.5 ± 1.3 (7)	29.0 ± 0.4 (5)
F2494A	4172 ± 806 (8)	3.4 ± 0.3 (8)	48.8 ± 6 (8)	13.5 ± 0.5 (9)	122 ± 29 (7)	35.0 ± 1.4 (6)	95.5 ± 15 (7)	30.4 ± 3.6 (7)	32.8 ± 0.7 (4)
M2493A, F2494A	Nonfunctional (11)				Nonfunctional (10)				

Data are mean  $\pm$  s.e.m. Numbers in parenthesis indicate *N* values.

\*Tau inactivation and percentage steady state current (%SS) measured at  $-60$  or  $-70$  mm Hg and  $-60$  mm Hg, respectively. %SS was measured as the ratio of  $I_{max}$  to residual current at the end of the 500ms pressure stimulus.

## Life Sciences Reporting Summary

Nature Research wishes to improve the reproducibility of the work that we publish. This form is intended for publication with all accepted life science papers and provides structure for consistency and transparency in reporting. Every life science submission will use this form; some list items might not apply to an individual manuscript, but all fields must be completed for clarity.

For further information on the points included in this form, see [Reporting Life Sciences Research](#). For further information on Nature Research policies, including our [data availability policy](#), see [Authors & Referees](#) and the [Editorial Policy Checklist](#).

### ▶ Experimental design

#### 1. Sample size

Describe how sample size was determined.

For electrophysiology, sample sizes represent the number of cells used for recordings and analysis. The sizes were chosen based on consistency and quality of data across conditions and multiple experiments.

#### 2. Data exclusions

Describe any data exclusions.

For patch clamp recordings, no data was excluded unless the recording quality was poor due to factors such as large noise or instability.

#### 3. Replication

Describe whether the experimental findings were reliably reproduced.

Electrophysiological experiments were reproduced according to the sample size as indicated in each figure. In addition, the recordings and parameters were reproducible across multiple days and transfection batches.

#### 4. Randomization

Describe how samples/organisms/participants were allocated into experimental groups.

For patch clamp recordings, samples were grouped based on the genes of interests transfected into the cells.

#### 5. Blinding

Describe whether the investigators were blinded to group allocation during data collection and/or analysis.

The investigators were not blinded to group allocation.

Note: all studies involving animals and/or human research participants must disclose whether blinding and randomization were used.

#### 6. Statistical parameters

For all figures and tables that use statistical methods, confirm that the following items are present in relevant figure legends (or in the Methods section if additional space is needed).

n/a Confirmed

- The exact sample size (*n*) for each experimental group/condition, given as a discrete number and unit of measurement (animals, litters, cultures, etc.)
- A description of how samples were collected, noting whether measurements were taken from distinct samples or whether the same sample was measured repeatedly
- A statement indicating how many times each experiment was replicated
- The statistical test(s) used and whether they are one- or two-sided (note: only common tests should be described solely by name; more complex techniques should be described in the Methods section)
- A description of any assumptions or corrections, such as an adjustment for multiple comparisons
- The test results (e.g. *P* values) given as exact values whenever possible and with confidence intervals noted
- A clear description of statistics including central tendency (e.g. median, mean) and variation (e.g. standard deviation, interquartile range)
- Clearly defined error bars

See the web collection on [statistics for biologists](#) for further resources and guidance.

## ► Software

Policy information about [availability of computer code](#)

### 7. Software

Describe the software used to analyze the data in this study.

For electrophysiology data analysis, we used Clampfit v10.6, GraphPad Prism v6, and Microsoft Excel.  
For EM work, we used Leginon, EMHP, gctf v0.5, MotionCor2, RELION v2.0, Chimera v1.11.2.  
For model building, refinement, and structural analysis, we used Coot v0.8.8, Phenix v1.12, HOLE v2.2, MolProbity, EMRinger, APBS, and PYMOL v1.7

For manuscripts utilizing custom algorithms or software that are central to the paper but not yet described in the published literature, software must be made available to editors and reviewers upon request. We strongly encourage code deposition in a community repository (e.g. GitHub). *Nature Methods* [guidance for providing algorithms and software for publication](#) provides further information on this topic.

## ► Materials and reagents

Policy information about [availability of materials](#)

### 8. Materials availability

Indicate whether there are restrictions on availability of unique materials or if these materials are only available for distribution by a for-profit company.

There is no restriction.

### 9. Antibodies

Describe the antibodies used and how they were validated for use in the system under study (i.e. assay and species).

9E11 anti- C Myc mouse antibody was purchased from and validated by Santa Cruz Biotechnology (sc-47694). Goat anti-mouse secondary antibody conjugated to Alexa Fluor 568 was purchased from and validated by Life Technologies (A11004).

### 10. Eukaryotic cell lines

a. State the source of each eukaryotic cell line used.

HEK293F cells were purchased from ATCC. HEK293T Piezo1 knockout cells were created in house using CRISPR-Cas9 system. The methods for generating the cell line has been published, and is described in detail in Lukacs 2015 (PMID: 26387913).

b. Describe the method of cell line authentication used.

The HEK293F cell line was authenticated by ATCC and no further authentication was performed. The HEK293T Piezo1 Knockout cells were validated as mentioned in Lukacs 2015.

c. Report whether the cell lines were tested for mycoplasma contamination.

HEK293F cell lines tested negative for mycoplasma. The HEK293T Piezo1 Knockout cells were not tested.

d. If any of the cell lines used are listed in the database of commonly misidentified cell lines maintained by [ICLAC](#), provide a scientific rationale for their use.

None of the cell lines used are listed in the database of commonly misidentified cell lines maintained by ICLAC.

## ► Animals and human research participants

Policy information about [studies involving animals](#); when reporting animal research, follow the [ARRIVE guidelines](#)

### 11. Description of research animals

Provide details on animals and/or animal-derived materials used in the study.

No animals were used in this study.

Policy information about [studies involving human research participants](#)

### 12. Description of human research participants

Describe the covariate-relevant population characteristics of the human research participants.

No human research participants were used in this study.